Protein Functional Cycle Viewed at Atomic Resolution: Conformational Change and Mobility in Nitrophorin 4 as a Function of pH and NO Binding[†,‡]

Dmitry A. Kondrashov, Sue A. Roberts, Andrzej Weichsel, and William R. Montfort*

Department of Biochemistry & Molecular Biophysics and Program in Applied Mathematics, University of Arizona, Tucson, Arizona 85721

Received August 5, 2004; Revised Manuscript Received August 24, 2004

ABSTRACT: The blood-sucking insect *Rhodnius prolixus* uses nitrophorin 4, a heme protein, to deliver nitric oxide (NO) to a victim, causing vasodilation and improved feeding. Binding of NO occurs at a ferric heme and is modulated by pH. NO binding at lower pH induces a large conformational change involving loops A−B and G−H that leads to distal pocket desolvation and protection of the nitrosyl heme complex. We have determined the crystal structures of *Rhodnius* nitrophorin 4 to ultrahigh resolution in four functional states: ±NO at pH = 7.4 and ±NO at pH = 5.6. The structure with NO at pH 7.4 (1.08 Å) is newly determined while the other complexes have been modeled to resolutions much greater than previously reported (1.0−0.85 Å). The ultrahigh resolution allowed us to resolve multiple conformers in binding-site loops, leading to a detailed description of the dynamics involved with storing NO in the insect salivary gland at low pH, and releasing NO in response to the increased pH of a victim's tissue. Strikingly, features for both the "open" and "closed" conformers exist under all conditions, suggesting that the flexible loops can transition with relative ease between conformational states. Yet, release of NO from rNP4 is much slower than found for other ferric heme proteins. The structures suggest that highly mobile loops can limit diffusion of diatomic molecules into and out of a protein cavity, a result with implications for the role of protein dynamics in function.

Many proteins undergo large changes in conformation while carrying out their functions. The need for conformational mobility became apparent with the very first protein structures of hemoglobin and myoglobin, which showed no unobstructed pathway from the solvent to the heme iron, suggesting that protein motion was required for oxygen binding. Since then, many proteins have been shown to change conformations, usually in response to ligand binding or change in environment. Often, two distinct conformations are observed, and the protein is described as a two-state system. More recently, experimental and theoretical studies have shown that proteins interchange between a multitude of conformational substates, but how structural fluctuations relate to protein function remains unclear.

A number of atomic resolution structures, loosely defined as those beyond 1.2 Å, have recently become available, contributing to an improved understanding of the nature and functional relevance of conformational heterogeneity (*1*). In particular, such structures reveal many residues to occupy more than one conformational state, and suggest that the motion between these states is linked with function (see, for example, the structures of cholesterol oxidase (*2*), calmodulin (*3*), and TIM (*4*)). Atomic resolution allows other, previously difficult, questions to be addressed as well, such as the protonation state of catalytic residues in the proteins subtilisin (*5*) and β-lactamase (*6*), and the distortion of a carbohydrate substrate on binding to endoglucanase CelA (*7*).

The subject of the present study is nitrophorin 4 from *Rhodnius prolixus* (rNP4).[1] Nitrophorins are nitric oxide (NO) transport proteins from the saliva of blood-feeding insects (*8*). *Rhodnius* nitrophorins, in the course of their function, are injected with saliva into the tissue of the victim, where NO is released and histamine binds in its place. Delivery of NO initiates a signaling cascade leading to vasodilation and reduced platelet aggregation, thereby improving the blood supply for the insect, while sequestration of histamine prevents inflammation associated with tissue damage, protecting the insect from detection. A ferric heme is used for both NO and histamine binding, taking advantage of the lower intrinsic affinity of NO for ferric heme ($K_d \sim 10^{-8}$ M) than ferrous heme ($K_d \sim 10^{-14}$ M). Seven such proteins have been isolated from the "kissing bug", *R. prolixus* (*9*−*11*).

NO, a ubiquitous signaling molecule in higher animals, is highly reactive, and the goal of numerous investigations is

[†] This work was supported in part by National Institutes of Health Grant HL62969 (to W.R.M.) and fellowships from NSF IGERT and the University of Arizona BIO5 (to D.A.K.). Portions of this research were carried out at the Stanford Synchrotron Radiation Laboratory, a national user facility operated by Stanford University on behalf of the U.S. Department of Energy. Diffraction data were also measured at BioCARS Sector 14, Advanced Photon Source, Argonne National Laboratory, which was supported by the U.S. Department of Energy under Contract No. W-31-109-Eng-38. Use of the BioCARS Sector 14 was supported by the National Institutes of Health, National Center for Research Resources, under Grant RR07707.

[‡] Coordinates for all structures reported have been deposited in the Protein Data Bank (PDB entries 1X8N, 1X8O, 1X8P, 1X8Q).

* To whom correspondence should be addressed: William R. Montfort, Department of Biochemistry& Molecular Biophysics, University of Arizona, 1041 E. Lowell St., Tucson, AZ 85721; tel, 520-621-1884; fax, 520-621-1697; e-mail, montfort@email.arizona.edu.

[1] Abbreviations: NO, nitric oxide; rNP4, *Rhodnius* nitrophorin 4.

10.1021/bi0483155 CCC: $27.50
Published on Web 10/08/2004

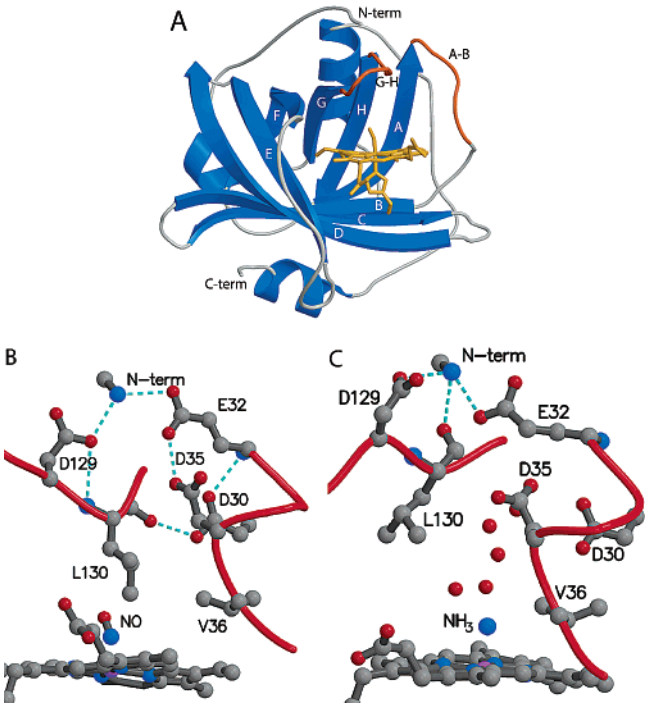

FIGURE 1: Ribbon diagrams of *Rhodnius* nitrophorin 4. (A) The β-barrel core (strands A−H) and surrounding helices are shown in blue. Loops A−B and G−H are indicated in orange. Heme, NO, and proximal ligand His 59 are shown in gold (ball-and-stick representation). (B) Closed conformer (rNP4−NO, pH 5.6) showing the hydrogen bonding network between carboxylic groups, the N-terminus, and the carbonyl of Leu 130. The side chains for Leu 130 and Val 36 are packed against NO in the binding pocket. (C) Open conformer (rNP4−NH_3, pH 7.4) showing the loss of hydrogen bonds among carboxylates, the new position for Leu 130 and its flipped carbonyl, and the alternate hydrogen bonding arrangement around the N-terminus.

to understand how the molecule is successfully handled by target proteins. In the nitrophorins, the NO molecule is protected from reaction while stored in the insect saliva, but released when the protein reaches the tissue of the victim. This is accomplished by sensing a change in pH: NO binding is tighter at the pH of the insect's saliva (~5) than at the pH of the tissue of a typical victim (~7.5) (*12*). Kinetic measurements of NO binding and release reveal that only the off rates are pH dependent, and, in general, are multiphasic and slow (*13*, *14*). The mechanism for this involves a large, pH dependent, conformational change (*14*, *15*).

Of the *Rhodnius* nitrophorins, rNP4 is particularly well suited for detailed structural analyses since it forms isomorphous crystals at low and high pH; its crystals diffract beyond 0.8 Å resolution; and NO binding, with subsequent change in protein conformation, does not harm the crystal. These features have led to several high-resolution structures of the protein (*15*−*17*), which revealed a closed conformation with NO trapped in a desolvated, hydrophobic pocket at low pH, and an open conformation after NO is released at high pH. The heme is highly distorted in these structures, more so on binding NO, a feature that may help prevent reduction of the heme by NO. The NO-induced conformational change at low pH is centered on two loops near the NO binding pocket, loops A−B (residues 30−37) and G−H (125−131), which connect β sheet strands A to B, and G to H, respectively (Figure 1A).

Both pH and ligand polarity are detected by the protein (*15*). At low pH, an extensive hydrogen bonding arrangement is observed involving 4 carboxyl groups, the Leu 130 carbonyl and the amino terminus (Figure 1B). At high pH, the carboxyl groups repel one another, the 130−131 peptide bond flips nearly 180°, a different set of hydrogen bonds forms, and loop A−B becomes highly disordered (Figure 1C). Mutation of the groups involved in these two arrangements leads to pH insensitive proteins (*14*). Ligand polarity is detected in the distal pocket itself. Hydrophobic ligands such as NO or CO induce hydrophobic residues Leu 130 and Val 36 to pack against the ligand, leading to expulsion of solvent from the pocket (Figure 1C), and producing a "hydrophobic trap" for NO (*15*, *18*). This occurs despite the high mobility of the A−B and G−H loops. Polar distal ligands such as cyanide or ammonia do not induce this conformation (*15*, *17*).

To gain further insight into this unusual mechanism, we have determined the structures of rNP4 to ultrahigh resolution for all four key steps in the binding, storage, and release of NO: ±NO at pH = 7.4 and ±NO at pH = 5.6. Of these, the rNP4−NO (pH 7.4) structure is presented for the first time, while the others have been determined to substantially increased resolutions. The results lead to a more detailed understanding of the structure and dynamics of the functionally important regions of the protein, and how this relates to NO storage and release in the nitrophorins.

MATERIALS AND METHODS

Protein Expression, Purification, and Crystallization. rNP4 was overexpressed in *Escherichia coli*, isolated from inclusion bodies, renatured, and crystallized as previously described (*13*, *15*, *19*). Crystals were grown at room temperature using the hanging drop method and prepared for data measurement under the following conditions. rNP4−NH_3 (pH 7.4) was grown in 2.8 M ammonium phosphate (pH 7.4), moved to a saturating ammonium phosphate solution for cryoprotection, retrieved with a cryoloop (Hampton), and flash frozen in liquid nitrogen. rNP4−NO (pH 5.6) was obtained by transferring a crystal grown at pH 7.4 to an ammonium phosphate solution at pH 5.6 that had first been deoxygenated with argon gas and then saturated with NO gas. The crystal was flash frozen after soaking for several minutes. rNP4−NO (pH 7.4) was prepared in the same manner, except for using a pH 7.4 soaking solution. rNP4−H_2O (pH 5.6) was grown in 22% PEG 4000 with 100 mM sodium citrate buffer, pH 5.6, and moved to a higher PEG concentration prior to freezing. These crystals are isomorphous with those grown in ammonium phosphate (space group C_2, cell constants a = 70.3 Å, b = 42.5 Å, c = 53.0 Å, β = 94.5°).

Data Measurement and Processing. Diffraction data for rNP4−H_2O (pH 5.6) and rNP4−NH_3 (pH 7.4) were measured on BIOCARS beamline 14-BMC of the Advanced Photon Source, Argonne National Laboratory, using an ADCS Quantum 4 detector. Diffraction maxima were seen to 0.75 Å; however, adequate completeness was only available to 0.85 Å resolution. Diffraction data for rNP4−NO (pH 5.6) and rNP4−NO (pH 7.4) were measured on beamlines 9-1 and 11-1, respectively, at SSRL, Stanford, using ADSC Quantum 315 detectors. These data were limited

Table 1: Crystallographic Data

	pH 5.6		pH 7.4	
	rNP4−H_2O	rNP4−NO	rNP4−NH_3	rNP4−NO
wavelength (Å)	0.9	0.751	0.9	0.980
temperature (K)	100	100	100	100
resolution (Å)	22−0.85	20−1.01	22−0.85	36−1.08
no. of reflns (total/unique)	362878/ 113651	304866/ 82359	425606/ 113853	364168/ 66157
multiplicity	3.2	3.7	4.0	5.5
completeness (%)[a]	80.7 (63.4)	98.8 (93.2)	82.8 (56.8)	98.4 (95.1)
$I/\sigma(I)$[a]	19.4 (2.4)	21.0 (6.5)	18.5 (1.8)	10.4 (1.8)
R_{merge}[a]	0.04 (0.23)	0.049 (0.18)	0.038 (0.32)	0.059 (0.27)

[a] Overall (last shell).

to 1.0 and 1.08 Å resolution. All data were reduced with d*trek (*20*) as incorporated into the CrystalClear software package (Rigaku Corporation), and CCP4 (*21*). Data statistics are summarized in Table 1.

Model Building and Refinement. Models were refined using SHELX 97-2 (*22*), with manual rebuilding using O (*23*). Previously determined rNP4 structures, including solvent, but without alternate conformers, were used as a starting point for each refinement, and the entire resolution range was used from the beginning. In the first stage, refinement was performed using isotropic *B*-factors, and large difference peaks that could be modeled as multiple conformers were added, as well as waters in favorable positions. In the next stage, anisotropic temperature factors were added, which reduced R_{free} by at least 0.03. This allowed more detailed modeling of disorder in protein residues, as well as further addition of solvent atoms. Hydrogens were added in calculated positions, based on the neutral pH protonation states, which produced a further drop in R_{free} of 0.01. More disorder could be modeled at this stage, primarily in residues with a weakly occupied alternate conformer, including certain weakly occupied water molecules. As a final step, we examined the possibility of relaxing the default restraints on distances, angles, and anisotropic *B*-factors, but found that this did not improve R_{free} and so retained the more stringent weighting factors.

The high resolution of the data allowed for clear identification of multiple conformations in many residues. Generally, a difference peak of at least 6σ ($\sim$0.5 $e^-/Å^3$) was considered necessary for addition of an alternate conformer to a residue. However, creating an alternate conformation for one atom sometimes required linked atoms to be added to the conformer in order to preserve reasonable stereochemistry, even when an alternate position was not indicated in electron density maps due to overlap with the primary position. Typically in such cases, the side chain shows obvious difference peaks but the main chain does not. As a rule, we included all of the main chain atoms in an alternate conformer if the β carbon was disordered, reasoning that the main chain geometry is likely subtly affected by the disorder even if no large difference peaks are present. Protein atoms had occupancies refined along with *B*-factors, whereas the solvent disorder had fixed occupancies (most at 0.5; 0.3 for weak waters) unless a solvent alternate conformer was clearly linked to disorder in the protein, in which case the water occupancy was the same as in the protein conformer. Where possible, residues that conflicted with one another's alternate conformers were also modeled with linked occupancies.

Table 2: Refinement Statistics

	pH 5.6		pH 7.4	
	rNP4−H_2O	rNP4−NO	rNP4−NH_3	rNP4−NO
refinement range (Å)	6−0.85	6−1.01	6−0.85	6−1.08
no. of atoms[a]				
protein	1635	1595	1628	1545
ligand/cofactor	44	50	45	46
solvent	361	395	360	321
data/param ratio	5.8	4.3	5.9	3.8
rmsd (Å)				
distances (target)	0.016 (0.02)	0.015 (0.02)	0.015 (0.02)	0.014 (0.02)
angles (target)	0.037 (0.04)	0.033 (0.04)	0.036 (0.04)	0.034 (0.04)
R_{cryst}/R_{free}	0.10/0.13	0.10/0.13	0.13/0.16	0.14/0.17

[a] Includes alternate conformations and partially occupied solvent molecules.

The high resolution of our structures allowed us to model small but functionally important deviations in certain bond lengths and angles from those in model compounds. In particular, heme nonplanarity, which is thought to influence its reduction potential, could be modeled by removing planar restraints, and the heme macrocycle was refined without any restraint for at least 10 cycles. One final cycle of block-diagonal full-matrix least-squares minimization (while holding other parameters fixed) was then performed for each structure to generate standard errors for distances and angles in the groups attached to the heme iron.

Refinement statistics are summarized in Table 2. Model quality was assessed using the program PROCHECK (*24*). All residues in all four structures displayed ϕ/ψ values in the favored or allowed regions of a Ramachandran plot. Heme distortion was estimated using normal coordinate structural decomposition (NSD) method developed by Shelnutt and co-workers (*25*). MOLSCRIPT (*26*), BOBSCRIPT (*27*), and RASTER3D (*28*) were used to prepare figures.

RESULTS

Rhodnius NP4 crystallizes into a single monoclinic crystal form at pH values between 5 and 8. The rNP4 crystals tolerate the pH-dependent changes in protein conformation that occur on binding NO, and diffract to beyond 0.8 Å resolution. These factors allowed us the unusual opportunity of studying a large protein conformational change at atomic resolution, without changes in crystal packing. Four structures are described: rNP4−H_2O (pH 5.6), rNP4−NO (pH 5.6), rNP4−NH_3 (pH 7.4), and rNP4−NO (pH 7.4). The resolution of these structures ranges from 1.08 to 0.85 Å (Tables 1 and 2), revealing a highly detailed description of the protein in multiple conformations. In what follows, we first summarize our general findings and then discuss features specific to each structure.

Overview of Crystallographic Results. The high resolution of the data allowed us to recognize multiple conformations for residues throughout the protein and to refine anisotropic temperature factors. Relaxing of standard stereochemical restraints was found not to be necessary, and not to lower R_{free}. The high resolution also allowed us, as a final step, to perform unrestrained full-matrix refinement to calculate estimated standard deviations for individual bond distances and angles. This was accomplished by using the DAMP option in SHELXL to freeze atomic positions.

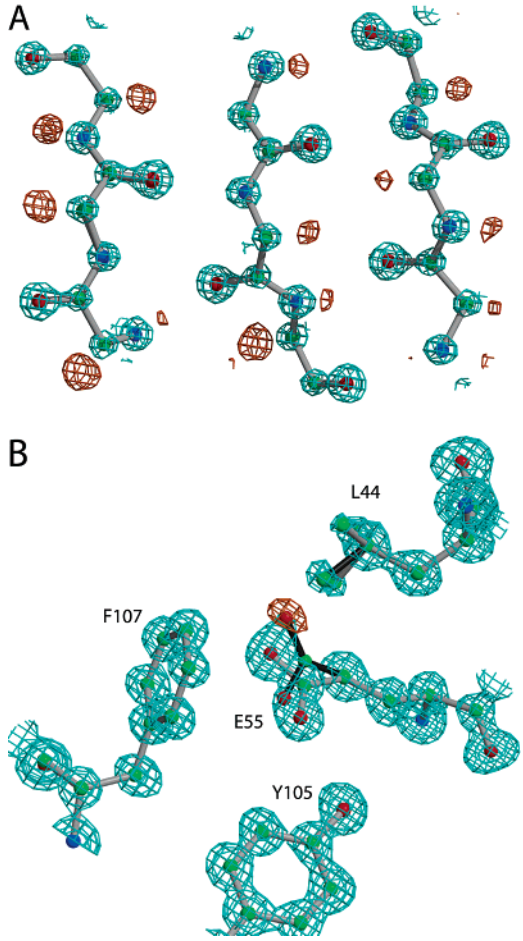

FIGURE 2: Electron density in the protein core of rNP4−NO (pH 5.6). (A) The backbone atoms of three β strands are shown (residues 110−112, 117−119, and 135−137). The blue electron density is from the final $2F_o - F_c$ map contoured at 5σ, while the orange electron density is from an $F_o - F_c$ map contoured at 2.8σ, using a model where backbone hydrogens were omitted and subsequently refined for several cycles. Note the consistently larger volume of the density peaks for nitrogen (blue) and oxygen (red) atoms, as compared with carbon atoms (green). The hydrogen peaks are not consistent in size, with some not appearing at this contour level. (B) A difference peak (orange contours) that appears to be in a hydrogen position is too large (6σ), based on analysis of the main-chain hydrogens, and so was modeled as an alternate conformer of Glu 55. The $2F_o - F_c$ map (cyan) is contoured at 2σ and the $F_o - F_c$ map at 3σ.

The resulting electron density maps are of excellent quality. In well-ordered parts of the protein, oxygen and nitrogen atoms display larger peaks than carbon atoms, and many hydrogen atoms can be seen (Figure 2A). All atoms are observed in all four structures except for a few surface side chains, and, in certain cases, residues 100 and 101, and loops A−B and G−H. The structures were very similar except in the distal pocket, where differences in pH and distal ligand led to multiple conformations for the A−B and G−H loops, many of which occurred simultaneously in a given crystal.

Multiple Conformations in a Single Crystal. The high resolution of our structures allowed alternate protein conformations to be detected and modeled for each crystal. Many of these were present under all conditions, but with differences in occupancy. This proved useful during model building, as a dominant conformer from one structure frequently fit the alternate electron density in another. This was particularly important for modeling loops A−B and G−H, which undergo a dramatic change in conformation between open and closed states.

Table 3: Residues in Multiple Conformations

	pH 5.6		pH 7.4	
	rNP4−H_2O	rNP4−NO	rNP4−NH_3	rNP4−NO
total[a]	35	27	29	23
entire residue	14	10	16	8
side chain only	14	10	13	8
G−H loop	7	7	0	7

[a] Does not include partially occupied solvent molecules.

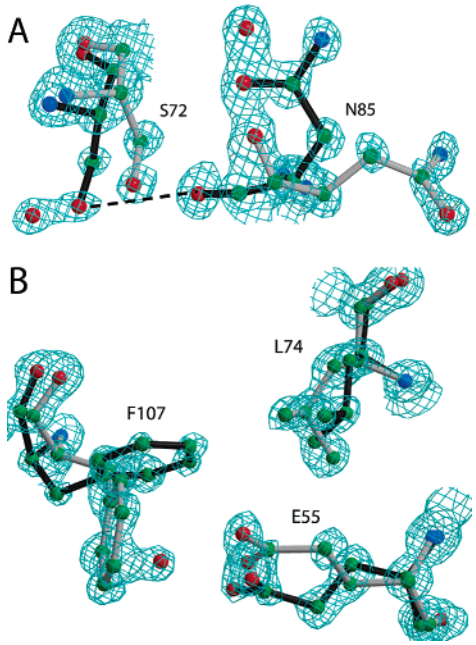

FIGURE 3: Concerted conformational changes at atomic resolution. (A) Two linked conformers are shown from rNP4−H_2O (pH 5.6). The predominant conformer is shown in gray and has an occupancy of ~0.57. A hydrogen bond (dashed line) between Asn 85 (CO) and Ser 72 (OH) occurs in the alternate conformation, while in the primary conformation this interaction is replaced by two partially occupied water molecules. The $2F_o - F_c$ map is contoured at 1.7σ. (B) Linked conformers in rNP4−NH_3 (pH 7.4). The predominant conformation, in gray, has an occupancy of ~0.57. Note again the partially occupied water, linked to the minor conformer. The $2F_o - F_c$ map is contoured at 2σ.

As many as 43 out of 184 residues were modeled in two conformational states in at least one structure and up to 35 in any given structure (Table 3); for most of the residues showing multiple conformations, disorder occurred in more than one structure. The alternate conformers vary from single atom displacements to the repositioning of entire loops. Occupancy values as low as 0.2 could be reliably modeled for individual atoms in the structures. In surface residues (lysines, serines, aspartates) the disorder was generally confined to side chain atoms. Elsewhere in the protein, alternate conformations involving backbone atoms were discovered, typically involving several interacting residues.

Of particular interest are neighboring residues with clearly linked multiple conformers, indicating their involvement in concerted conformational changes. For example, residues Ser 72 and Asn 85, along with ordered solvent molecules, shift together in all four structures (Figure 3A). Likewise, buried residue Glu 55 moves in concert with Leu 77, Phe 107, Thr

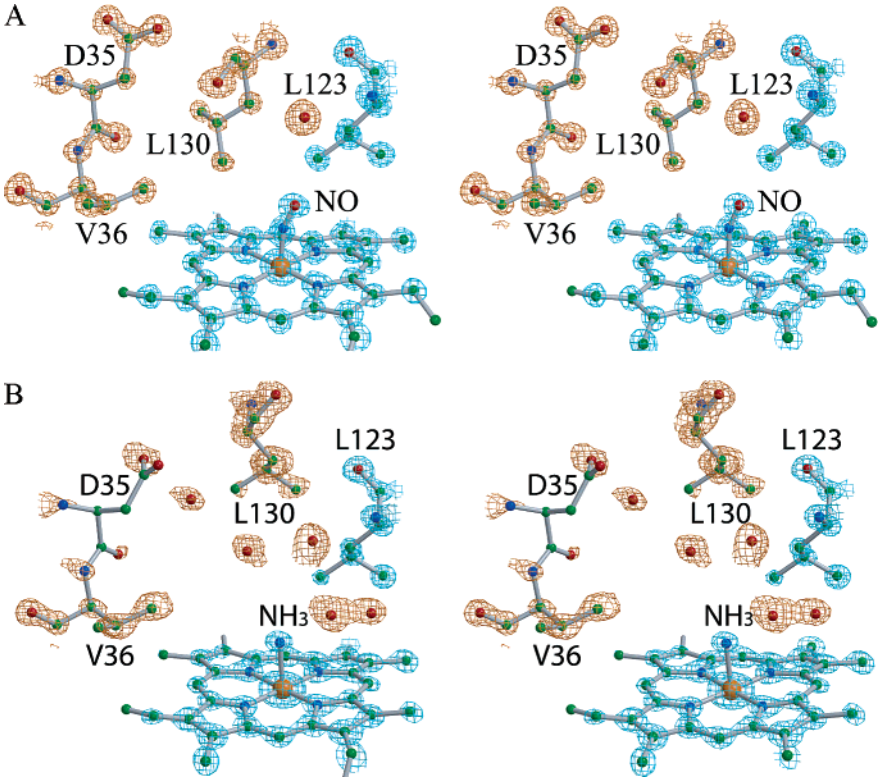

FIGURE 4: Stereoview of electron density in the distal pocket. (A) Closed conformer in rNP4−NO (pH 5.6). Shown is electron density in the final $2F_o - F_c$ map for the heme, NO, and Leu 123 at 3.0σ (cyan), and for Asp 35, Val 36 (A−B loop), and Leu 130 (G−H loop) at 2.0σ (orange). The side chains of Leu 130, Asp 35, and Val 36 are well ordered and packed into the binding pocket, against NO. (B) Open conformer in rNP4−NH_3 (pH 7.4). Electron density is shown at 3.0σ (cyan) and 1.5σ (orange). Leu 130 has left the distal pocket, leaving room for 5 or more solvent molecules. The A−B loop is poorly ordered under these conditions; however, Val 36 clearly partially occupies the position associated with the closed conformer.

121, and solvent (Figure 3B). Linked multiple conformations for the A−B and G−H loops were also readily apparent and are discussed in detail below.

rNP4−NO at pH 5.6. We extended the resolution of this structure to 1.0 Å from that previously reported (1.1 Å) and improved the model quality, leading to a decrease in R_{free} from 0.15 to 0.13. The NO ligand, distal pocket, and loops in the closed conformer are quite clear in the final electron density map (Figure 4A). The NO displays a bending motion toward the back of the distal pocket, as previously described (*17*), leading to a large anisotropic component in the oxygen *B*-factor. The equivalent isotropic temperature factors for the nitrogen and oxygen atoms were 5.5 and 9.7 Å^2, respectively. These values are slightly higher than those for the heme and His 59, which have $B = 4-5$ Å^2, but are similar to atoms in van der Waals contact with the NO moiety ($B = 7-9$ Å^2). Nonetheless, a small difference peak remains next to the NO in the final electron density map, suggesting that either additional disorder takes place in the NO or contacting residues or the occupancy of NO is slightly less than 100%. At present, we cannot distinguish between these possibilities.

Under these conditions (pH 5.6, NO bound) the closed conformer predominates, serving to protect the NO molecule. The A−B and G−H loops covering the distal pocket remain dynamic, however, and display higher temperature factors than for the rest of the protein, leading us to suggest that the protection of NO is more from a nonpolar phase separation that resembles a dynamic oil droplet than from a solid, unvarying conformation that blocks escape (*15*). In the present work, we found that, in addition to the dynamic behavior about the closed conformation, the G−H loop (residues 125−131) also visits the open conformation. One of the most striking differences between conformations is that peptide bond 130−131 flips 180°, causing Leu 130 to move away from the distal pocket. Difference electron density peaks were found that coincide directly with atomic positions for the flipped-open conformer and associated ordered solvent, leading to the modeling of both open and closed conformers in the protein (Figure 5A). The minor conformer refined to an occupancy of 0.29. Inclusion of the alternate conformation led to a 0.005 decrease in the value for R_{free}.

rNP4−NH_3 at pH 7.4. This structure was extended from 1.15 to 0.85 Å and R_{free} reduced by 0.04. The distal ligand is ammonia (from the crystallization precipitant (*16*)), and the distal pocket holds several water molecules, including some with alternate positions (Figure 4B). Previously, positions for the A−B loop could not be identified at all in this structure. With the increased resolution, it became clear that the closed position for the loop was significantly occupied (Figure 4B). That other conformations also occur was equally clear due to the poor quality of the electron density and the existence of relatively strong residual difference peaks near prolines 33 and 37 (about 0.6 e^-/Å^3) that we were unable to model. Nonetheless, Val 36, which stabilizes contacts between NO and Leu 130, is clearly sampling the closed conformation in the absence of NO. In contrast, loop G−H lies completely in the open conformer. No extra electron density arising from the closed conformer is visible in difference electron density maps (Figure 5D).

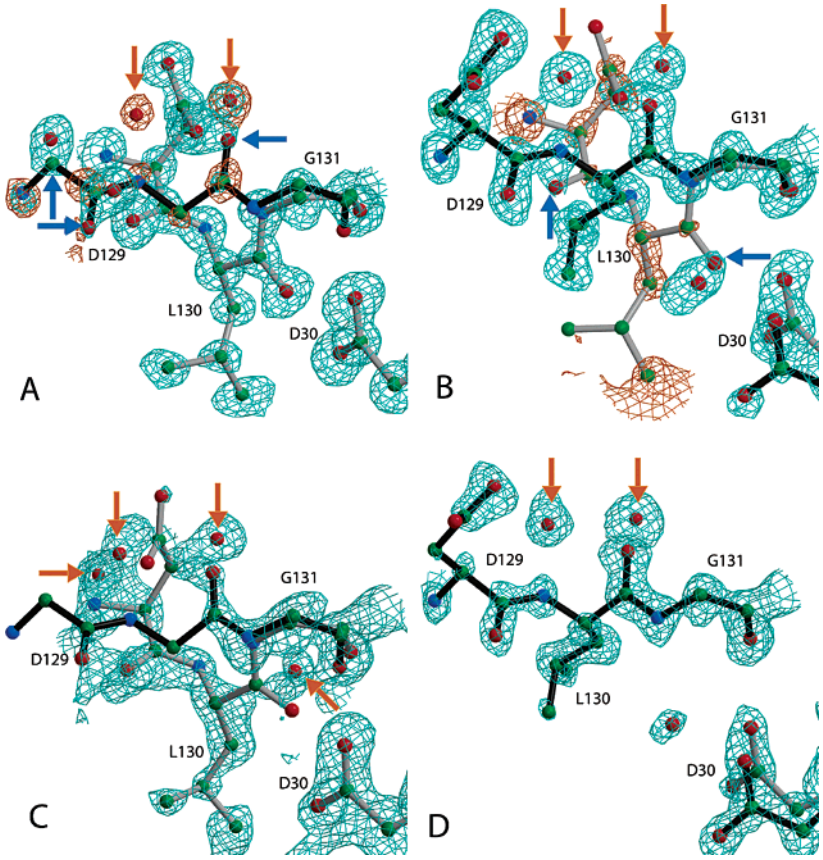

FIGURE 5: Multiple conformers and disorder in the loop region. Shown are parts of loop G−H (Asp 129, Leu 130, Gly 131), and loop A−B (Asp 30). The closed conformer is shown with gray bonds, while the open conformer is shown with black bonds. Partially occupied water molecules that are associated with only one of two conformers are indicated with red arrows. Extended features in the electron density centered on one conformer, but attributable to the other conformer, are indicated with blue arrows. (A) rNP4−NO (pH 5.6). The closed conformer is dominant ($2F_o - F_c$ map in cyan, 1.3σ). A difference map (orange, 2σ) computed from a model before the alternate (open) conformer was introduced indicates the presence of the open conformer and associated water structure. Only the backbone atoms of the open conformer are shown. (B) rNP4−H_2O (pH 5.6). Predominant conformations switch: the open conformer and associated solvent is dominant ($2F_o - F_c$ map in cyan, 1.4σ), but the unbiased difference map (orange, 2.2σ) indicates that the closed conformer is weakly present. Asp 30 is seen to be in two conformations, apparently not correlated with disorder in loop G−H. (C) rNP4−NO (pH 7.4). The electron density ($2F_o - F_c$, 1.4σ) suggests a high degree of mobility for loop G−H that is difficult to model with just two conformers. For example, Leu 130 shows features of both the open (position of the carbonyl group) and the closed (position of the side chain) conformers. (D) rNP4−NH_3 (pH 7.4). Only the open conformation is observed for loop G−H ($2F_o - F_c$, 1.4σ), although with weaker density than in part B, suggesting greater dynamics. Asp 30 displays two conformations, confirming its independence of loop G−H.

rNP4−H_2O at pH 5.6. The aqua complex at pH 5.6 responds to a mixture of competing influences for open and closed conformers. The low pH favors the closed conformer, but the aqua ligand favors the open complex. We extended this structure from 1.4 Å resolution to 0.85 Å, and lowered R_{free} from 0.25 to 0.13. Loop A−B is less well ordered than in the NO complex at pH 5.6, but predominantly resides in the closed conformation. Residues 33−34 show the greatest disorder, while Glu 32, Asp 35, and Val 36 are clearly indicated in the closed position. Loop G−H also occupies both conformations, but, in contrast, predominantly resides in the open state. The major conformer has the carbonyl of Leu 130 rotated away from Asp 30 and hydrogen bonded to the amino terminus, and the loop backbone is shifted. Evidence for the closed conformer appears most clearly in difference electron density maps (Figure 5B). Inclusion of the closed conformer in the model, with a final occupancy of 0.28, led to a reduction in R_{free} of 0.005. Further evidence for the closed conformer comes from Asp 30, which also displays two conformations. The predominant position is consistent with carbonyl 130 lying in the flipped open position, but the minor position is consistent with carbonyl 130 forming a hydrogen bond with Asp 30. The distal pocket displays ordered water molecules, one of which is coordinated to the heme.

rNP4−NO at pH 7.4. The NO complex at pH 7.4 also has two competing influences, but in the opposite direction: the NO ligand favors the closed conformer while the higher pH favors the open conformer. This structure, first reported herein, has substantial disorder in both loops. Loop A−B has poor electron density, and residues 33−35 in particular are difficult to model. Residues Glu 32 and Val 36 have weak density consistent with the closed conformation. Loop G−H, which displays aspects of both open and closed conformers in roughly equal proportion, is poorly modeled at present despite the availability of high resolution (1.08 Å). This is likely reflected in the relatively high R_{free} for the structure (0.17). The multiple conformers are particularly apparent in residues 129−131 (Figure 5C), where the carbonyl of Leu 130 has better density for the open position, within hydrogen bonding distance of the amino terminus, while the side chain of Leu 130 has observable density only for the closed conformer, where it is packed against the NO molecule. Inclusion of both conformers lowered R_{free} slightly

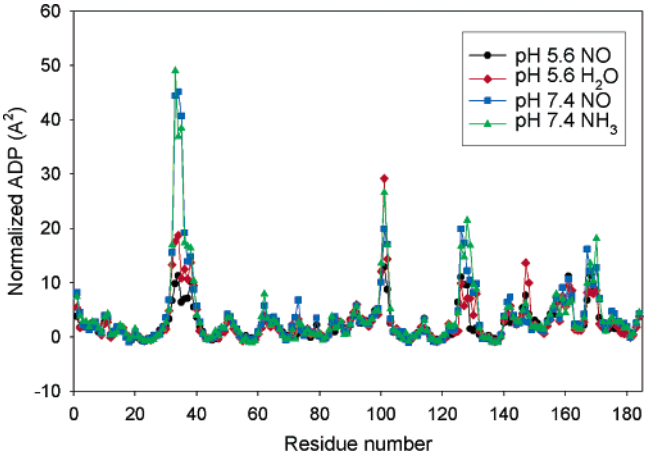

FIGURE 6: Normalized carbon α isotropic ADPs by residue. The agreement between the four structures is very close except in loops A−B and G−H (32−36 and 126−131).

(0.003); however, there is smeared electron density near Asp 129 that is not well addressed in the model, and the electron density for residues 127−128 is largely missing. Despite this, two conformers were required for the entire loop in order to obtain an acceptable model. NO ligation is clearly indicated in the distal pocket; however, its geometry is consistent with photoreduction occurring during data measurement. The more open distal pocket has several ordered water molecules in place, which may contribute to reduction of the nitrosylated heme, as previously noted for mutant forms of rNP4 with modified loops (*14*).

Temperature Factors as a Measure of Dynamics. To compare the mobility of different parts of the protein, we examined crystallographic temperature factors, also known as atomic displacement parameters (ADPs), which measure variance in atomic position. To correct for differences in crystal ordering and data measurement, ADPs from each structure were normalized relative to a set of Cα atoms from 44 core residues by subtracting the mean of the reference set from each ADP (Figure 6). These adjusted temperature factors show very close agreement among the four independent structures, with the exception of the loops A−B and G−H and residues 100 and 101. We also performed a comparison of anisotropic ADPs, which can indicate the primary direction of atomic motion. We used the method of Merritt (*29*) to quantify the similarity of the anisotropic tensors between corresponding carbon α atoms in the four structures; the results (not shown) again displayed close agreement in all parts of the protein except for loops A−B and G−H. The similarity of both magnitude and direction of motion in the invariant parts of the protein indicates that the conformational change near the binding site has no discernible global impact on protein motion.

Observation of Hydrogens. We tested our ability to recognize hydrogen atoms in the two pH 5.6 structures and found that the data do not allow for consistent hydrogen detection. We used difference electron density maps where main chain hydrogen atoms were omitted (carbon α and amide atoms from 184 residues) and compared those with difference maps from the complete model (with hydrogens), to exclude noise peaks. Using a cutoff level of 2.5σ, we found 86 and 88 carbon α hydrogens, and 52 and 50 amide hydrogens, in the NO and H_2O complexes, respectively. The highest peak was 5.4σ, which corresponds to ~0.45 $e^-/Å^3$ in absolute density. There is limited agreement between the two sets: 57 carbon α hydrogens and 26 amide hydrogens are seen in both structures. These findings are consistent with the 0.66 Å structure of aldose reductase (R_{free} = 0.093) that was recently reported by Podjarny and co-workers (*30*). In that study, 54% of all hydrogens were found using a cutoff level of 1σ.

Table 4: Heme Distortion

	pH 5.6		pH 7.4	
	rNP4−H_2O	rNP4−NO	rNP4−NH_3	rNP4−NO
Fe−ligand[a]	2.055(6)	1.69(1)	2.043(9)	1.74(2)
N−O		1.09(1)		1.20(2)
Fe−N−O		159.1(1.1)		143.8(1.6)
Fe−His	1.942(5)	1.994(7)	1.975(7)	2.06(1)
Fe−NA	1.978(6)	1.964(9)	1.975(9)	1.98(1)
Fe−NB	1.996(7)	1.994(9)	1.983(9)	1.99(1)
Fe−NC	2.009(6)	2.001(9)	1.989(9)	1.98(1)
Fe−ND	1.979(7)	1.986(8)	1.99(1)	1.97(1)
B2u (saddling)[b]	0.30	0.37	0.33	0.29
B1u (ruffling)	−0.55	−0.81	−0.64	−0.76

[a] Final distances and errors determined through unrestrained full-matrix refinement (distances in angstroms, angles in degrees). [b] Deviations along heme normal modes calculated with NSD.

The residues with observed hydrogen peaks are almost all in the most ordered regions of the protein. For the NO complex, virtually all peaks are on atoms with *B*-factors below 7 $Å^2$, and for the H_2O structure, below 9 $Å^2$; however, even highly ordered atoms do not consistently display hydrogens (see Figure 2A). This analysis allowed us to better interpret certain difference electron density peaks, such as one near buried Glu 55 (Figure 2B). The *B*-factors on the side chain are higher than the threshold value, and the peak is higher than any observed hydrogen atom belonging to the main chain, which led us to interpret the peak as an alternate conformer. Thus, the observation of hydrogens on the most functionally interesting side chains is precluded unless they are particularly well ordered.

Unrestrained Refinement. The ultrahigh resolution of the data allowed for unrestrained refinement of geometric parameters in functionally important locations. In particular, the geometry of the heme and associated ligands changes with the oxidation state of the heme iron and the nature of the coordinating ligands, and the geometry of carboxyl groups changes with protonation state. Unrestrained iron coordination geometry was previously evaluated (at lower resolution) for the rNP4−NO (pH 5.6) and rNP4−NH_3 (pH 7.4) complexes (*17*), where the heme was found to be ruffled under both conditions, but more so on binding NO, a π-acceptor ligand, and the Fe−NO bond was found to be bent away from the expected linear arrangement, but to have the expected bond length. Similar geometries were found in the higher resolution structures of these complexes (Table 4). In the NO complex, the Fe−NO bond length (1.69 Å) was again consistent with a ferric nitrosyl complex, as intended, but the Fe−NO bond angle (159°) was again bent away from the linear arrangement (*31*). However, computational analyses suggest that NO is easily deformed away from a linear bond, in this case by Leu 123 and Leu 133, which flank the NO molecule (Stepanian, S. G., Adamowicz, L., and Montfort, W. R., in preparation).

Table 5: Bond Lengths (C−O1 and C−O2) from Unrestrained Refinement of Carboxyl Groups[a]

	pH 5.6 H_2O		pH 7.4 NH_3		pH 5.6 NO		pH 7.4 NO	
Asp 21	1.24(1)	1.27(1)	1.25(1)	1.25(1)	1.25(1)	1.25(1)	1.25(2)	1.27(2)
Asp 27	1.23(1)	1.26(1)	1.24(1)	1.28(1)	1.25(1)	1.25(1)	1.22(2)	1.28(2)
Asp 30[b]	nm[c]	nm	nm	nm	1.24(2)	1.30(2)	nm	nm
Asp 61	1.24(1)	1.26(1)	*1.18(2)*	1.30(2)	1.27(1)	1.27(1)	1.25(2)	1.26(2)
Asp 70[b]	1.20(1)	1.31(1)	1.20(1)	1.32(1)	1.20(1)	1.33(1)	1.19(2)	1.35(2)
Glu 77	1.27(1)	1.27(1)	1.25(1)	1.26(1)	1.24(1)	1.27(1)	1.23(2)	1.28(2)
Asp 132	1.23(1)	*1.29(1)*	1.22(1)	1.25(1)	1.24(1)	1.27(1)	1.20(2)	1.28(2)
Asp 174	1.25(1)	*1.29(1)*	1.24(2)	1.29(2)	1.25(1)	1.29(2)	1.23(3)	1.30(2)
heme PA	1.22(1)	1.24(1)	*1.18(1)*	1.26(1)	1.23(1)	1.25(1)	1.24(2)	1.25(2)

[a] Restraints for bond lengths and angles of well-ordered carboxyl groups (*B*-factors < 15 Å^2 in all structures) were removed for several refinement cycles, followed by block-matrix inversion for errors (in parentheses). Expected bond length is 1.25 Å for unprotonated group; values deviating by greater than 3σ are in italics. [b] Bond lengths for protonated Asp 70 are expected to be 1.2 (C═O) and 1.3 (C−OH) Å. [c] Not measurable due to disorder.

In rNP4−NO (pH 7.4), the Fe−NO bond distance (1.74 Å) and angle (144°) indicate that the heme has been photoreduced to the ferrous state (Fe(II)) during data measurement. A similar result was found in mutant forms of rNP4 that destabilized the closed conformer (*14*), suggesting that photoreduction of the iron nitrosyl complex is more facile when solvated then when isolated from water in the closed conformer. Photoreduction could only affect the iron coordination sphere, and not the protein structure, since it occurred while the protein was frozen at 100 K. Additionally, the pH 5.6 structure of rNP4(Fe(II))−NO, produced through chemical heme reduction, is nearly identical to the Fe(III) structure (Maes, E. M., and Montfort, W. R., in preparation).

Heme geometry was analyzed for distortion along normal modes using the program NSD (*25*); we report the results for the two main modes, ruffling and saddling, in Table 4. As previously noted (*17*), the rNP4 heme is highly distorted, particularly with respect to ruffling, which increases on binding NO to roughly the same extent at both pH values. Saddling, in contrast, is not increased on NO binding.

We also performed unrestrained refinement of several carboxyl groups, to determine their protonation state. Deprotonated carboxylates are expected to be symmetric, with C−O bond lengths near 1.25 Å, while protonated carboxylic acids should have bond lengths of ∼1.3 Å for the protonated oxygens and ∼1.2 Å for the double-bonded oxygens. We investigated the most ordered carboxyl groups (*B*-factors < 15 Å^2 in all structures), and found that solvent-exposed groups had C−O bond lengths near the ideal distance of 1.25 Å, under all four conditions, with only 4 bond lengths (out of 56) differing by more than 3σ (Table 5). We also considered carboxyl groups that might be protonated. Asp 70 is buried and hydrogen bonded to a buried solvent molecule, and to a heme propionate. In all four structures, the C−O bond of the oxygen near the propionate was longer (1.33 ± 0.02 Å) than the oxygen near the water (1.20 ± 0.01 Å), while the propionate oxygens were symmetric (1.24 ± 0.02 Å), indicating that the hydrogen in the hydrogen bond resides on Asp 70. Asp 30 in the NP4−NO (pH 5.6) structure forms a hydrogen bond with the carbonyl of Leu 130, and so it must be protonated. The carboxyl bond lengths of 1.30 Å (for C−OH in a hydrogen bond with Leu 130) and 1.24 Å (C═O, Table 5) are consistent with this conclusion.

DISCUSSION

We have determined crystal structures of NP4 to ultrahigh resolution in all four functional states of the protein, yielding an atomic model for a full protein cycle that includes a large ligand-induced conformational change. The dynamic behavior of proteins, from which function emerges, is difficult to model by X-ray crystallography, since only conformations that are well occupied in the crystal give rise to interpretable changes in the diffraction pattern. Given ultrahigh resolution, however, many minor conformations are readily apparent, and modeling of these provides insight into the dynamics of the protein, which in turn speaks to function. Perhaps the most striking observation in the present study is that the protein visits all conformations under all conditions, with highly occupied conformations under one set of conditions becoming minor—but still recognizable—conformations under other conditions. The implications of these data for NO binding, transport, and release are considered below.

Advantages and Limitations of Atomic Resolution. The structures presented herein are to resolutions between 0.85 and 1.08 Å. Diffraction data for the two lower pH structures were better and yielded the better overall crystallographic *R*-factors (R_{free} = 0.13 vs 0.16 and 0.17 for the higher pH structures). Building and refining structures where multiple minor conformations can be discerned is considerably more time-consuming than for standard structure determinations. In our hands, this extra effort led to two major results. First, we were able to model minor conformations that contribute to function, particularly in the loops that regulate NO binding and release (Table 3, Figures 3 and 5). For example, the position for loop A−B could not be discerned at all in prior structures of rNP4−NH_3 at 1.1 Å resolution, but can be seen to partially occupy the closed conformer in the present structure at 0.85 Å. Second, we were able to refine the iron coordination geometry without model restraints, and the overall heme geometry without planar restraints, which led to more accurate estimates of bond lengths, bond angles, and macrocycle distortion (Table 4). The latter is important since the protein matrix distorts the heme away from the lowest energy conformation (planar), presumably to stabilize the Fe(III)−NO complex. Despite these advances, it is clear that there is more information in the "disordered" regions than can be currently modeled with discrete conformers (Figure 5). Possibly a model with a weighted distribution of positions for highly mobile groups might capture the crystal structure more accurately.

Directly identifying hydrogens in our models was less successful. One desirable outcome of high-resolution structure determinations is the identification of functionally important hydrogen atoms. To test our ability to identify hydrogens, we refined two of the models without hydrogen atoms at backbone positions, and asked whether electron density peaks of 2.5σ or greater were present in difference electron density maps. Using this conservative approach, only ~38% of backbone hydrogen atoms were identified, leading us to conclude that our models are not sufficiently reliable to allow direct identification of hydrogen atoms in any but the best of cases. Other studies, where higher resolution or lower *R*-factors could be achieved, and using less stringent criteria, have reported finding 54−80% of the expected hydrogens (*5*, *6*, *32*, *33*).

More promising, however, was our ability to identify protonated oxygens in carboxyl groups, which differ in length by ~0.1 Å from the unprotonated oxygen. This analysis clearly indicated, for the first time, which oxygens were protonated in a series of hydrogen bonds involving heme propionate, Asp 70, and a buried water molecule (Table 5). Thus, at 1.0 Å resolution, unrestrained refinement of bond geometry can reliably indicate subtle—but functionally important—differences in chemical state, such as protonation or metal oxidation state.

The Effect of pH and NO Binding on the Distal Pocket Loops. The two functionally significant loops, A−B and G−H, display markedly different behavior in response to NO binding and pH changes. Loop A−B is well ordered in the "closed" conformer that occurs on binding NO at pH 5.6, but shows degraded electron density in the three other structures, where the "open" configuration predominates. There is no evidence for a single conformation for the A−B loop in the open state, suggesting that it is highly mobile when not in the closed conformer. The A−B loop has only limited direct contact, through Val 36, with the binding cavity in the closed conformer, while four acidic residues (Asp 30, Glu 32, Asp 35, and Asp 129) come together in the closed conformation and destabilize the closed A−B loop position at higher pH values. Thus, the A−B loop is better ordered in the rNP4−H_2O (pH 5.6) structure than in the rNP4−NO (pH 7.5) structure.

In contrast, loop G−H adopts two well-defined conformers, both of which apparently occur to some degree under all conditions. The transition from the open to the closed state is analogous to the folding process, combining the hydrophobic collapse around NO with the formation of specific hydrogen bonds. NO binding and pH play different roles: the hydrophobic desolvation of the binding cavity is presumably the main positive driving force for closure, leading to Leu 130 packing against the NO molecule, while deprotonation of carboxylic groups at neutral pH serves to disrupt the closed state. Without NO, loop G−H remains primarily in the open conformation regardless of pH, since there is no hydrophobic "core" for Leu 130 to pack against. In the presence of NO, pH plays a major role: at pH 7.5, rNP4−NO exhibits a complex and disordered behavior, responding to the closing influence of a hydrophobic cavity and to the opening influence of negatively charged carboxylate groups in close proximity, along with the inability to form the Asp 30−Leu 130 hydrogen bond.

Similar observations of multiple positions for functionally important loops have been recently reported for other proteins. In cholesterol oxidase, the 0.9 Å structure without the steroid substrate revealed weakly occupied conformations for active site residues that correspond to the conformation seen at lower resolution for the steroid complex of the enzyme (*2*). As in the present data, improved resolution showed that both functionally important conformations can be occupied under one set of conditions. Likewise, the TIM−PGA structure at 0.85 Å revealed multiple conformers for mobile loop 6, which plays a key role in substrate binding and catalysis (*4*). Ultrahigh-resolution structures such as these suggest that nearly isoenergetic conformations are common in functionally important regions of proteins.

Role of Loop Dynamics in Controlling NO Binding and Release. NO dissociation from rNP4 is multiphasic and slow under all conditions. The slower phase at pH 5 has k_{off} = 0.02 s^{-1}, which increases to 0.6 s^{-1} at pH 8 (*13*, *14*). Mutation of the A−B or G−H loops leads to proteins that have lost the pH dependence for NO release, but still display multiphasic and slow kinetic behavior (*14*). In contrast, ferric (met) myoglobins from elephant, sperm whale, and horse heart display monophasic NO release with rate constants in the range of 10−40 s^{-1} (*34*, *35*), despite having buried distal pockets.

How, then, is rNP4 able to trap NO so much more effectively than metmyoglobin? The *Rhodnius* nitrophorins and the metmyoglobins use the same heme and have similar nitrosyl vibrational spectra (*18*, *36*, *37*), suggesting that nitrosyl bond strength is similar in both protein families, despite the highly distorted heme in the nitrophorins. Access to the distal pocket is regulated in both cases; however, rNP proteins would seem to have the more accessible distal pockets due to the highly dynamic loops guarding the distal pocket. The structural data presented herein make it clear that, even at low pH and in the presence of saturating NO, the A−B and G−H loops are among the most dynamic portions of the protein, visiting both open and closed conformations. Nonetheless, that these dynamic loops can influence release is made clear by the mutagenesis studies mentioned above.

Insight into how this might be possible comes from three other approaches. First, photolysis studies coupled to IR spectroscopy of NO at very low temperatures indicate that the rNP4 binding pocket prevents NO diffusion away from the distal pocket after breakage of the Fe−NO bond, giving rise to a large geminate rebinding activity (*18*). The low quantum yield for NO photolysis at room temperature is also consistent with geminate rebinding (*13*). In myoglobin, pockets exist that facilitate diffusion by CO, and presumably O_2 and NO, away from the distal pocket, using pathways between the pockets that transiently open due to protein dynamics (*38*−*45*). These factors are thought to greatly reduce geminate recombination. In rNP4, such migration is apparently precluded, despite the existence of suitable pockets in the protein (*18*).

Molecular dynamics approaches are also useful for understanding NO trapping by rNP4. Simulations of CO migration in metmyoglobin show the molecule diffusing through the protein and residing in the experimentally identified pockets (*46*). Similar simulations with rNP4, however, show the NO molecule spending much greater time

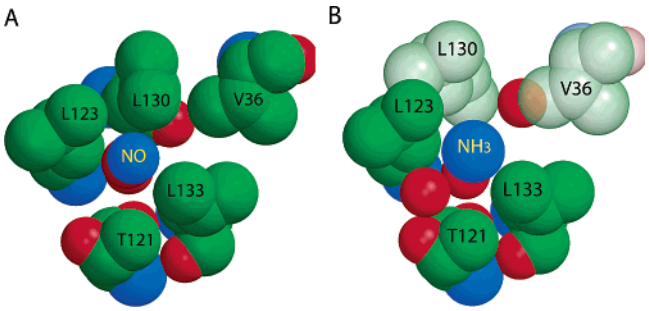

FIGURE 7: CPK rendering of the heme pocket (view from the distal heme side). (A) Closed conformer. NO resides in a closely packed hydrophobic environment. (B) Open conformer. Leu 130 has moved away from the ligand, and several additional water molecules are observed in the pocket. Note that Leu 130 and Val 36 are substantially more mobile in the open conformer, and they only partially occupy the positions shown, which is indicated by transparent rendering.

in the distal pocket (Kondrashov, D. A, and Montfort, W. R., in preparation). Despite extensive dynamics in and near the pocket, pathways for NO escape are infrequent, leading to enhanced geminate recombination.

Additional insight into this mechanism comes from a theoretical examination of the escape processes for a diffusing particle in a one-dimensional cavity with a fluctuating gate on one boundary (Kondrashov, D. A., Watkins, J. C., and Montfort, W. R., in preparation). The addition of geminate rebinding to such a system gives rise to new properties: escape can be slow and multiphasic, with observed rates dependent on both the gate opening rate and the probability of geminate rebinding, rather than being simply limited by the opening rate.

Taken together, these factors suggest the *Rhodnius* nitrophorins function somewhat like an oil droplet to keep NO in the distal pocket. Dynamic loops, like the individual molecules of oil in a droplet, continually move but provide a thermodynamic barrier to water penetration. The tight packing of oily side chains (Figure 7A), which fluctuate but do not open diffusion passages, encourages geminate rebinding, which is ultimately the main factor in preventing NO escape. The role of rebinding is crucial, due to the slow rate of breaking of the NO−Fe bond (milliseconds) (*47*) compared with the rates of diffusion (pico- to nanoseconds). Disruption of the closed conformer at higher pH (Figure 7B) leads to solvation of the binding pocket, removal of the thermodynamic barrier to NO escape, and an increase in the escape rates by a factor of 30. Even at pH 7.5, however, the loops are partially closed, which may contribute to the still slower NO escape rates for rNP4 than for metmyoglobins.

The atomic resolution structures presented here contributed to a detailed understanding of the mechanism of small-ligand retention by a protein. The evidence of dynamic loop behavior belies the simpler model of rNP4 as an open or closed cage, instead suggesting the nuanced picture described above.

ACKNOWLEDGMENT

We thank Jacquie Brailey for her assistance in protein preparation and Abreeza Zegeer for her assistance with crystal growth.

REFERENCES

1. Vrielink, A., and Sampson, N. (2003) Sub-Angstrom resolution enzyme X-ray structures: is seeing believing? *Curr. Opin. Struct. Biol. 13*, 709−715.
2. Lario, P. I., Sampson, N., and Vrielink, A. (2003) Sub-atomic resolution crystal structure of cholesterol oxidase: what atomic resolution crystallography reveals about enzyme mechanism and the role of the FAD cofactor in redox activity, *J. Mol. Biol. 326*, 1635−1650.
3. Wilson, M. A., and Brunger, A. T. (2000) The 1.0 Å crystal structure of Ca(2+)-bound calmodulin: an analysis of disorder and implications for functionally relevant plasticity, *J. Mol. Biol. 301*, 1237−1256.
4. Kursula, I., and Wierenga, R. K. (2003) Crystal structure of triosephosphate isomerase complexed with 2-phosphoglycolate at 0.83-Å resolution, *J. Biol. Chem. 278*, 9544−9551.
5. Kuhn, P., Knapp, M., Soltis, S. M., Ganshaw, G., Thoene, M., and Bott, R. (1998) The 0.78 Å structure of a serine protease: *Bacillus lentus* subtilisin, *Biochemistry 37*, 13446−13452.
6. Minasov, G., Wang, X., and Shoichet, B. K. (2002) An ultrahigh resolution structure of TEM-1 β-lactamase suggests a role for Glu166 as the general base in acylation, *J. Am. Chem. Soc. 124*, 5333−5340.
7. Guerin, D. M., Lascombe, M. B., Costabel, M., Souchon, H., Lamzin, V., Beguin, P., and Alzari, P. M. (2002) Atomic (0.94 A) resolution structure of an inverting glycosidase in complex with substrate, *J. Mol. Biol. 316*, 1061−1069.
8. Montfort, W. R., Weichsel, A., and Andersen, J. F. (2000) Nitrophorins and related antihemostatic lipocalins from *Rhodnius prolixus* and other blood-sucking arthropods, *Biochim. Biophys. Acta 1482*, 110−118.
9. Andersen, J. F., Gudderra, N. P., Francischetti, I. M., Valenzuela, J. G., and Ribeiro, J. M. (2004) Recognition of anionic phospholipid membranes by an antihemostatic protein from a blood-feeding insect, *Biochemistry 43*, 6987−6994.
10. Champagne, D. E., Nussenzvieg, R. H., and Ribeiro, J. M. C. (1995) Purification, partial characterization and cloning of nitric oxide-carrying heme proteins (nitrophorins) from salivary glands of the blood-sucking insect *Rhodnius prolixus*, *J. Biol. Chem. 270*, 8691−8695.
11. Moreira, M. F., Coelho, H. S., Zingali, R. B., Oliveira, P. L., and Masuda, H. (2003) Changes in salivary nitrophorin profile during the life cycle of the blood-sucking bug Rhodnius prolixus, *Insect Biochem. Mol. Biol. 33*, 23−28.
12. Ribeiro, J. M. C., Hazzard, J. M. H., Nussenzveig, R. H., Champagne, D. E., and Walker, F. A. (1993) Reversible binding of nitric oxide by a salivary heme protein from a bloodsucking insect, *Science 260*, 539−541.
13. Andersen, J. F., Ding, X. D., Balfour, C., Shokhireva, T. K., Champagne, D. E., Walker, F. A., and Montfort, W. R. (2000) Kinetics and equilibria in ligand binding by nitrophorins 1−4: Evidence for stabilization of a NO−ferriheme complex through a ligand-induced conformational trap, *Biochemistry 39*, 10118−10131.
14. Maes, E. M., Weichsel, A., Andersen, J. F., Shepley, D., and Montfort, W. R. (2004) Role of binding site loops in controlling nitric oxide release: structure and kinetics of mutant forms of nitrophorin 4, *Biochemistry 43*, 6679−6690.
15. Weichsel, A., Andersen, J. F., Roberts, S. A., and Montfort, W. R. (2000) Reversible nitric oxide binding to nitrophorin 4 from *Rhodnius prolixus* involves complete distal pocket burial, *Nat. Struct. Biol. 7*, 551−554.
16. Andersen, J. F., Weichsel, A., Balfour, C. A., Champagne, D. E., and Montfort, W. R. (1998) The crystal structure of nitrophorin 4 at 1.5 Å resolution: Transport of nitric oxide by a lipocalin-based heme protein, *Structure 6*, 1315−1327.
17. Roberts, S. A., Weichsel, A., Qiu, Y., Shelnutt, J. A., Walker, F. A., and Montfort, W. R. (2001) Ligand-Induced Heme Ruffling and Bent NO Geometry in Ultra-High-Resolution Structures of Nitrophorin 4, *Biochemistry 40*, 11327−11337.
18. Nienhaus, K., Maes, E. M., Weichsel, A., Montfort, W. R., and Nienhaus, G. U. (2004) Tracking photolyzed NO in Nitrophorin 4 with Fourier Transform Infrared Spectroscopy, *J. Biol. Chem. 279*, 39401−39407.
19. Andersen, J. F., Champagne, D. E., Weichsel, A., Ribeiro, J. M. C., Balfour, C. A., Dress, V., and Montfort, W. R. (1997) Nitric oxide binding and crystallization of recombinant nitrophorin I, a

nitric oxide transport protein from the blood-sucking bug *Rhodnius prolixus*, *Biochemistry 36*, 4423−4428.
20. Pflugrath, J. W. (1999) The finer things in X-ray diffraction data collection, *Acta Crystallogr. D55*, 1718−1725.
21. Collaborative Computational Project Number 4. (1994) The CCP4 Suite: Programs for Protein Crystallography, *Acta Crystallogr. D50*, 760−763.
22. Sheldrick, G. M., and Schneider, T. R. (1997) SHELXL: High-Resolution Refinement, *Methods Enzymol. 277*, 319−343.
23. Jones, T. A., Zou, J. Y., Cowan, S. W., and Kjelgard, M. (1991) Improved methods for building protein models in electron density maps and the location of errors in these models, *Acta Crystallogr. A47*, 110−119.
24. Laskowski, R. A., MacArthur, M. W., Moss, D. S., and Thorton, J. M. (1993) PROCHECK: A program to check the stereochemical quality of protein structures, *J. Appl. Crystallogr. 26*, 283−291.
25. Jentzen, W., Song, X.-Z., and Shelnutt, J. A. (1997) Structural Characterization of Synthetic and Protein-Bound Porphyrins in Terms of the Lowest-Frequency Normal Coordinates of the Macrocycle, *J. Phys. Chem. B. 101*, 1684−1699.
26. Kraulis, P. J. (1991) MOLSCRIPT: A program to produce both detailed and schematic plots of protein structures, *J. Appl. Crystallogr. 24*, 946−950.
27. Esnouf, R. M. (1997) An extensively modified version of MolScript that includes greatly enhanced coloring capabilities, *J. Mol. Graphics Modell. 15*, 132−134, 112−113.
28. Merritt, E. A., and Murphy, M. E. P. (1994) Raster3D Version 2.0−A Program for Photorealistic Molecular Graphics, *Acta Crystallogr. D50*, 869−873.
29. Merritt, E. A. (1999) Comparing anisotropic displacement parameters in protein structures, *Acta Crystallogr. D55*, 1997−2004.
30. Howard, E. I., Sanishvili, R., Cachau, R. E., Mitschler, A., Chevrier, B., Barth, P., Lamour, V., Van Zandt, M., Sibley, E., Bon, C., Moras, D., Schneider, T. R., Joachimiak, A., and Podjarny, A. (2004) Ultrahigh resolution drug design I: details of interactions in human aldose reductase-inhibitor complex at 0.66 Å, *Proteins 55*, 792−804.
31. Scheidt, W. R., and Ellison, M. K. (1999) The synthetic and structural chemistry of heme derivatives with nitric oxide ligands, *Acc. Chem. Res. 32*, 350−359.
32. Esposito, L., Vitagliano, L., Sica, F., Sorrentino, G., Zagari, A., and Mazzarella, L. (2000) The ultrahigh resolution crystal structure of ribonuclease A containing an isoaspartyl residue: hydration and sterochemical analysis, *J. Mol. Biol. 297*, 713−732.
33. Jelsch, C., Teeter, M. M., Lamzin, V., Pichon-Pesme, V., Blessing, R. H., and Lecomte, C. (2000) Accurate protein crystallography at ultra-high resolution: valence electron distribution in crambin, *Proc. Natl. Acad. Sci. U.S.A. 97*, 3171−3176.
34. Sharma, V. S., Traylor, T. G., Gardiner, R., and Mizukami, H. (1987) Reaction of nitric oxide with heme proteins and model compounds of hemoglobin, *Biochemistry 26*, 3837−3843.
35. Laverman, L. E., Wanat, A., Oszajca, J., Stochel, G., Ford, P. C., and van Eldik, R. (2001) Mechanistic studies on the reversible binding of nitric oxide to metmyoglobin, *J. Am. Chem. Soc. 123*, 285−293.
36. Maes, E. M., Walker, F. A., Montfort, W. R., and Czernuszewicz, R. S. (2001) Resonance Raman spectroscopic study of nitrophorin 1, a nitric oxide-binding heme protein from *Rhodnius prolixus*, and its nitrosyl and cyano adducts, *J. Am. Chem. Soc. 123*, 11664−11672.
37. Ding, X. D., Weichsel, A., Andersen, J. F., Shokhireva, T. K., Balfour, C., Pierik, A. J., Averill, B. A., Montfort, W. R., and Walker, F. A. (1999) Nitric oxide binding to the ferri- and ferroheme states of nitrophorin 1, a reversible NO-binding heme protein from the saliva of the blood-sucking insect, *Rhodnius prolixus*, *J. Am. Chem. Soc. 121*, 128−138.
38. Schlichting, I., and Chu, K. (2000) Trapping intermediates in the crystal: ligand binding to myoglobin, *Curr. Opin. Struct. Biol. 10*, 744−752.
39. Brunori, M., and Gibson, Q. H. (2001) Cavities and packing defects in the structural dynamics of myoglobin, *EMBO Rep. 2*, 674−679.
40. Austin, R. H., Beeson, K. W., Eisenstein, L., Frauenfelder, H., and Gunsalus, I. C. (1975) Dynamics of ligand binding to myoglobin, *Biochemistry 14*, 5355−5373.
41. Tilton, R. F., Jr., Kuntz, I. D., Jr., and Petsko, G. A. (1984) Cavities in proteins: structure of a metmyoglobin−xenon complex solved to 1.9 Å, *Biochemistry 23*, 2849−2857.
42. Nienhaus, K., Deng, P., Kriegl, J. M., and Nienhaus, G. U. (2003) Structural dynamics of myoglobin: spectroscopic and structural characterization of ligand docking sites in myoglobin mutant L29W, *Biochemistry 42*, 9633−9646.
43. Ostermann, A., Waschipky, R., Parak, F. G., and Nienhaus, G. U. (2000) Ligand binding and conformational motions in myoglobin, *Nature 404*, 205−208.
44. Srajer, V., Ren, Z., Teng, T. Y., Schmidt, M., Ursby, T., Bourgeois, D., Pradervand, C., Schildkamp, W., Wulff, M., and Moffat, K. (2001) Protein conformational relaxation and ligand migration in myoglobin: a nanosecond to millisecond molecular movie from time-resolved Laue X-ray diffraction, *Biochemistry 40*, 13802−13815.
45. Schotte, F., Lim, M., Jackson, T. A., Smirnov, A. V., Soman, J., Olson, J. S., Phillips, G. N., Jr., Wulff, M., and Anfinrud, P. A. (2003) Watching a protein as it functions with 150-ps time-resolved x-ray crystallography, *Science 300*, 1944−1947.
46. Bossa, C., Anselmi, M., Roccatano, D., Amadei, A., Vallone, B., Brunori, M., and Di Nola, A. (2004) Extended molecular dynamics simulation of the carbon monoxide migration in sperm whale myoglobin, *Biophys. J. 86*, 3855−3862.
47. Hoshino, M., Ozawa, K., Seki, H., and Ford, P. C. (1993) Photochemistry of nitric oxide adducts of water-soluble iron(III) porphyrin and ferrihemoproteins studied by nanosecond laser photolysis, *J. Am. Chem. Soc. 115*, 9568−9575.

BI0483155